


Article

Dual-Engineering Tailored Co_3O_4 Hollow Microspheres Assembled by Nanosheets for Boosting Oxygen Evolution Reaction

Yinghan Cui ¹, Shiduo Yang ^{1,*}, Jianqiang Zhu ¹, Zaidong Wang ¹, Sen Chen ¹, Jian Qi ^{2,3,*}  and Huan Wang ^{1,*}

¹ Hebei Key Laboratory of Flexible Functionals Materials, School of Materials Science and Engineering, Hebei University of Science and Technology, Shijiazhuang 050000, China; cuiyh066@outlook.com (Y.C.); 19832218054@163.com (J.Z.); wanghbkjstu@163.com (Z.W.); neu_cs@163.com (S.C.)

² State Key Laboratory of Biochemical Engineering, Institute of Process Engineering, Chinese Academy of Sciences, Beijing 100190, China

³ School of Chemical Engineering, University of Chinese Academy of Sciences, Beijing 100049, China

* Correspondence: qzsd1233@163.com (S.Y.); jqj@ipe.ac.cn (J.Q.); wanghuanp@163.com (H.W.)

Abstract: The development of efficient, low-cost electrocatalysts for the oxygen evolution reaction (OER) is crucial for advancing sustainable hydrogen production through water splitting. This study presents a dual-engineering strategy to enhance the OER performance of Co_3O_4 by synthesizing hollow microspheres assembled from nanosheets (HMNs) with abundant oxygen vacancies and highly active crystal facet exposure. Through a modified one-step hydrothermal process, Co_3O_4 HMNs with exposed (111) and (100) crystal facets were successfully fabricated, demonstrating superior OER activity compared to Co_3O_4 nanocubes (NCs) with only (100) facet exposure. The optimized Co_3O_4 -5% HMNs exhibited a low overpotential of 330 mV at 10 mA cm^{-2} and a Tafel slope of 69 mV dec^{-1} . The enhanced performance was attributed to the synergistic effects of crystal facet engineering and defect engineering, which optimized the Co-O bond energy, increased the number of active sites, and improved conductivity. The unique hollow structure further facilitated mass transport and prevented nanosheet stacking, exposing more edge sites for catalytic reactions. This work highlights the potential of geometric and electronic structure modulation in designing high-performance OER catalysts for sustainable energy applications.

Keywords: oxygen evolution reaction; hollow microspheres; dual-engineering strategy; oxygen vacancies; active crystal facet



Academic Editors: Xingcai Wu and Lu Lu

Received: 22 April 2025

Revised: 11 May 2025

Accepted: 13 May 2025

Published: 16 May 2025

Citation: Cui, Y.; Yang, S.; Zhu, J.; Wang, Z.; Chen, S.; Qi, J.; Wang, H. Dual-Engineering Tailored Co_3O_4 Hollow Microspheres Assembled by Nanosheets for Boosting Oxygen Evolution Reaction. *Molecules* **2025**, *30*, 2181. <https://doi.org/10.3390/molecules30102181>

Copyright: © 2025 by the authors. Licensee MDPI, Basel, Switzerland. This article is an open access article distributed under the terms and conditions of the Creative Commons Attribution (CC BY) license (<https://creativecommons.org/licenses/by/4.0/>).

1. Introduction

Amid growing energy crises and environmental pollution, hydrogen energy has regained global attention [1–5]. Electrolytic water hydrogen production technology can not only convert fluctuating wind and solar energy into hydrogen energy but also achieve zero CO_2 emissions during the hydrogen production process, while the produced hydrogen has a purity of over 99.9% [6–10]. However, the efficiency of hydrogen production by electrolytic water is hindered by the sluggish oxygen evolution reaction (OER) [11–16], a complex four-electron-proton process [17,18]. Although commercial catalysts like RuO_2 and IrO_2 are effective, their scarcity and high-cost limit large-scale use [19–21]. Developing high-performance, low-cost non-precious metal OER catalysts is thus crucial for reducing hydrogen production costs and improving efficiency. Co_3O_4 , with its tunable electronic structure that is capable of breaking OER scaling relationships, is a promising candidate [22–24]. However, challenges such as low intrinsic activity and limited active

sites persist [25–27]. Addressing these issues requires strategic geometric and electronic structure modulation to enhance catalytic performance. This research aims not only to address the existing problems of Co_3O_4 -based catalysts but also to assist in developing highly efficient and affordable OER catalysts. These catalysts are expected to accelerate the widespread use of sustainable hydrogen energy.

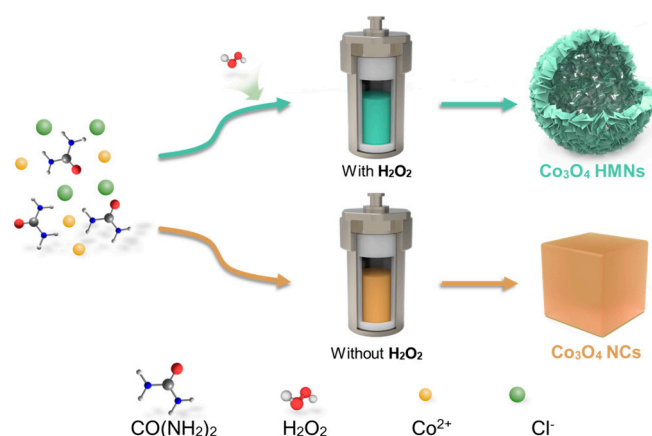
The fabrication of superstructure platforms, and in particular, hollow structures, can further expose a greater number of catalytic sites, expedite reactant transportation, and enhance the OER performance [28,29]. Moreover, crystal facet engineering and defect engineering modulation can further unlock the potential of materials and enhance their catalytic performance [30,31]. On the one hand, crystal facet engineering focuses on controlling the exposure of specific crystal facets. Different crystal facets possess distinct atomic arrangements and surface energies, resulting in varied chemical reactivities and physical properties [32,33]. By preferentially exposing the most active crystal facets, the catalytic performance of materials can be significantly enhanced. On the other hand, defect engineering involves intentionally introducing defects (such as vacancies, heteroatoms, etc.) into the lattice, which can effectively regulate the electronic structure and increase the activity of active sites [34–36].

This study presents a groundbreaking approach to enhance the performance of Co_3O_4 -based catalysts for the OER. Through the innovative integration of defect engineering and crystal facet engineering into a modified one-step hydrothermal process, Co_3O_4 hollow microspheres assembled by nanosheets (HMNs) were successfully synthesized. This unique synthesis method enables precise control over oxygen vacancies and the exposure of highly active crystal facets by simply adjusting the amount and concentration of hydrogen peroxide. The resultant Co_3O_4 HMNs, with exposed (111) and (100) crystal facets, demonstrated a remarkable boost in OER activity, outperforming traditional Co_3O_4 nanocubes (NCs) with only (100) crystal facet exposure. The superior performance can be attributed to the dual-engineering modulation strategy. On one hand, this strategy optimizes the Co-O bond energy, enhances reactant adsorption, and improves material conductivity, thereby significantly enhancing the intrinsic catalytic activity. On the other hand, it effectively increases the number of active sites on Co_3O_4 , further enhancing the overall catalytic performance. This novel synthesis of Co_3O_4 HMNs not only paves the way for more efficient electrocatalytic water splitting in hydrogen production but also holds great potential for applications in diverse energy-related fields, including metal-air batteries and rechargeable fuel cells.

2. Results and Discussion

Co_3O_4 HMNs and Co_3O_4 NCs were fabricated via a modified one-step hydrothermal process; the typical synthesis process is displayed in Scheme 1. The key distinction between the synthesis processes of Co_3O_4 HMNs and Co_3O_4 NCs lies in the strategic introduction of hydrogen peroxide (H_2O_2) as a critical reaction modulator (Scheme 1). Specifically, the formation of HMNs relies on the H_2O_2 -assisted Ostwald ripening mechanism. In the modified one-step hydrothermal process, H_2O_2 interacts with cobalt-salt and urea precursors. Its strong oxidizing property oxidizes cobalt ions and controllably dissolves parts of the initial cobalt-containing precursors for oxidative etching. As the reaction proceeds, the dissolved substances accumulate and recrystallize under the reaction temperature conditions. Oxidative-etching-induced local differences make recrystallization likely to occur in the form of hollow structures, with atoms/molecules arranging in an orderly manner to yield nanosheet-assembled hierarchical hollow microspheres on an existing structure. The synergy of oxidative etching and recrystallization provides substances/templates for recrystallization and yields a stable hollow structure, which can prevent nanosheet stacking,

expose active sites, offer transport channels, and boost the material's performance in OER applications [37,38]. In contrast, the NC synthesis pathway deliberately excludes H_2O_2 , favoring instead a direct nucleation–growth mechanism that produces solid crystalline nanoparticles through conventional thermal decomposition routes.



Scheme 1. Schematic diagram of the synthesis of Co_3O_4 HMNs and Co_3O_4 NCs.

The surface morphology and microstructural characteristics of the synthesized samples were initially investigated using scanning electron microscopy (SEM). Figures 1a and S2a,b present SEM images of Co_3O_4 HMNs synthesized from precursor solutions containing different hydrogen peroxide concentrations (3%, 5% and 7%). The SEM images (Figures 1a and S2a,b) reveal that all synthesized samples exhibited well-defined microsphere architectures, which were hierarchically constructed from interconnected nanosheets. Furthermore, transmission electron microscopy (TEM) was employed to observe the internal geometric structure of the synthesized sample. The TEM image (Figure 1b) reveals that the microspheres, assembled from nanosheets, exhibited a hollow structure interspersed with numerous channels. These channels can facilitate efficient mass transport of reactants and products [39,40]. The construction of HMNs can avoid the stacking of Co_3O_4 nanosheets, thereby exposing more edge sites and increasing effective contact with the electrolyte [41,42]. Previous research has indicated that edge sites exhibit higher electrocatalytic activity [43]. Furthermore, the construction of HMSs can shorten the electron transfer path, thereby enhancing the OER kinetics [44,45]. Next, an X-ray photoelectron spectroscopy (XPS) survey scan was performed to determine the elemental composition of the sample. The XPS survey spectra (Figure S3) of the Co_3O_4 -5% HMNs and Co_3O_4 NC samples clearly showed the presence of Co and O, as indicated by their characteristic photoelectron peaks. To further observe and measure the shape and size of the nanosheets assembled into microspheres, a TEM image of Co_3O_4 -5% HMNs was further magnified (Figure 1c). The TEM images (Figure 1c) shows that the nanosheet had a polygonal shape with a thickness of approximately 22 nm. To elucidate the exposed crystal facets of these nanosheets, high-resolution transmission electron microscopy (HRTEM) images were acquired (Figure 1d,e). The HRTEM images (Figure 1d,e) revealed that the lateral facet of the nanosheet was indexed to the (111) crystal facet of Co_3O_4 , while the basal plane corresponded to the (100) crystal facet of the Co_3O_4 . These findings not only confirmed the single-crystal nature of the Co_3O_4 nanosheet but also revealed that the nanosheet predominantly exposed the (111) and (100) crystal facets, highlighting its well-defined crystallographic orientation. Theoretical and experimental studies have revealed that high-index facets possess a greater density of dangling bonds and higher surface energy, which will contribute to the improvement of catalytic performance [46,47]. In addition, it can be seen from the selected area electron diffraction (SAED) image (Figure 1f) that there were numerous bright spots distributed on

the diffraction ring, mainly due to the fact that the selected region included multiple single crystal nanosheets.

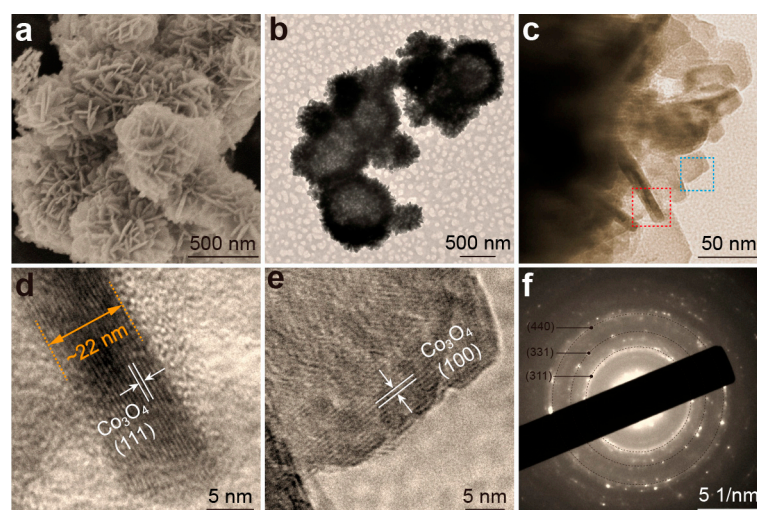


Figure 1. Co_3O_4 -5% HMNs: (a) SEM image; (b) TEM image; (c) High magnification TEM images; (d,e) are the HRTEM images corresponding to the parts in the red and blue dashed boxes of Figure 1c, respectively; (f) SAED image.

As a comparison, Co_3O_4 nanocubes (NCs) with only exposed (100) crystal facets were also synthesized. First of all, a precursor solution without added hydrogen peroxide was prepared (Figure 1). Subsequently, Co_3O_4 NCs were successfully synthesized through the same hydrothermal process. The SEM image in Figure 2a shows that Co_3O_4 NCs had a cubic morphology and a smooth surface. A TEM image (Figure 2b) further revealed that the interior of the cubic nanocrystals was a solid structure with no internal cavities. Due to the symmetry of the structure, Co_3O_4 NCs exposed the same (100) crystal facet, which was confirmed by the HRTEM image shown in Figure 2c. Figure 2d presents a schematic diagram of the Co_3O_4 NCs derived from the aforementioned analytical characterization data, demonstrating the distinctive architectural features of Co_3O_4 NCs. The successful synthesis of Co_3O_4 NCs allowed us to undertake a systematic investigation into the facet-dependent properties and their crucial roles in electrocatalytic processes.

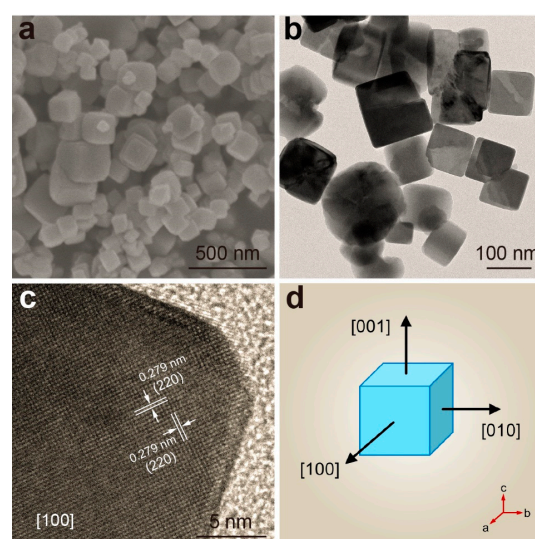


Figure 2. Co_3O_4 NCs: (a) SEM image; (b) TEM images; (c) HRTEM image; (d) Schematic representation of Co_3O_4 NCs; note: [abc] is an index of a specified crystal axis.

Due to the fact that HMNs are assembled from a large number of nanosheets, a large number of pores of different sizes form, which play an important role in the diffusion and adsorption of reactants. Therefore, studying the specific surface area and pore distribution of the samples is beneficial for exploring differences in material properties. Next, nitrogen adsorption–desorption measurements were conducted to study the specific surface area and pore distribution of the samples. Figure 3a displayed the nitrogen adsorption–desorption isotherms for both Co_3O_4 -5% HMNs and Co_3O_4 NCs. The specific surface areas were calculated using the Brunauer-Emmett-Teller (BET) method based on the corresponding isotherm data [48]. The results show that Co_3O_4 HMNs had a specific surface area of $42.6 \text{ m}^2 \text{ g}^{-1}$, i.e., larger than Co_3O_4 NCs ($8.2 \text{ m}^2 \text{ g}^{-1}$). This indicated that Co_3O_4 -5% HMNs could expose more effective surfaces to the electrolyte, thereby increasing the probability of contact between active sites and reactants. This result further confirmed the structural advantages of HMNs. Moreover, the pore distribution curves in Figure 3b show that the Co_3O_4 -5% HMNs had more pores, and these pore sizes were mainly around 5–50 nm, while Co_3O_4 NCs had fewer pores, with a pore size range concentrated between 3 and 20 nm. More pores and larger pore sizes facilitate the diffusion of the electrolyte, thereby accelerating the reaction kinetics process. Afterwards, X-ray diffraction (XRD) patterns were collected to further investigate the phase composition and structural characteristics of the cobalt oxides. The XRD patterns presented in Figures 3c and S4 demonstrate that Co_3O_4 HMNs and Co_3O_4 NCs exhibited diffraction peaks that precisely matched the reference pattern of cubic phase Co_3O_4 (PDF#: 43-1003, space group: Fm-3m) [49,50]. This complete correspondence in peak positions and relative intensities confirmed the phase purity of both materials without detectable impurities. Fourier transform infrared spectroscopy (FTIR) measurements were conducted to investigate structural modifications in the materials by analyzing the characteristic vibrational modes of chemical bonds. As shown in Figure 3d, the absorption peaks at ~ 585 and $\sim 665 \text{ cm}^{-1}$ in the FTIR spectra were attributed to the stretching vibration of Co-O bands [51,52]. It could be clearly distinguished from the FTIR spectra that the absorption peak of Co_3O_4 -5% HMNs had a red shift compared to Co_3O_4 NCs. The observed red shift in the absorption peaks of Co_3O_4 -5% HMNs suggested a significant weakening of Co-O bonds within the spinel structure. This bond weakening induced an upward shift of the O 2p band toward the Fermi level, thereby facilitating enhanced oxygen ion mobility and more efficient oxygen exchange processes [53–55]. Consequently, these structural modifications contributed to improving the OER kinetics through accelerated surface redox processes.

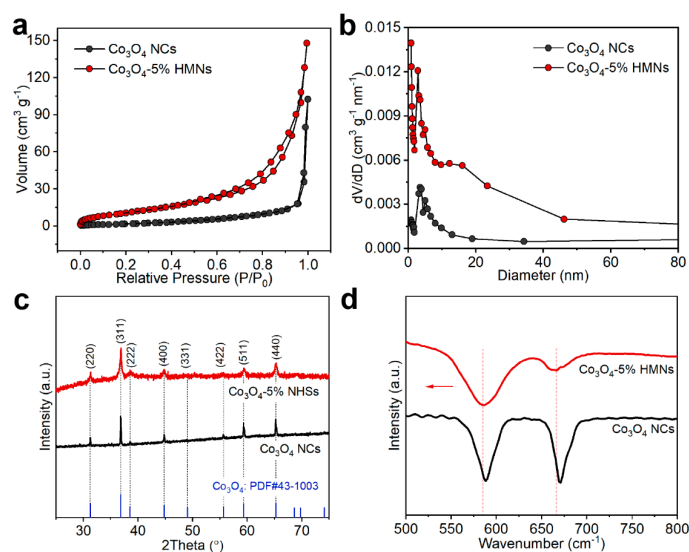


Figure 3. Co_3O_4 -5% HMNs and Co_3O_4 NCs: (a) Nitrogen adsorption–desorption isotherms, (b) pore distribution curves, (c) XRD patterns, (d) FTIR spectra.

The electrocatalytic reaction mainly occurs on the surface of a catalyst, so studying the surface properties of a catalyst is of great significance for clarifying the catalytic reaction mechanism. In our study, XPS, as a surface-sensitive technique with a typical probing depth of 3–10 nm, was employed to characterize the chemical environments and electronic structures of surface elements, providing critical insights into the morphological features and defect chemistry of the electrocatalysts. The Co 2p spectra of Co₃O₄ NCs and Co₃O₄-5% HMNs were further analyzed by peak fitting (Figure 4a,b). In the Co 2p spectrum (Figure 4a) of Co₃O₄ NCs, the characteristic absorption peaks at approximately 796.19 eV (u_0), 781.10 eV (v_0), 794.59 eV (u), and 779.59 eV (v) were assigned to Co²⁺ 2p_{1/2}, Co²⁺ 2p_{3/2}, Co³⁺ 2p_{1/2}, and Co³⁺ 2p_{3/2}, respectively, confirming the coexistence of Co³⁺ and Co²⁺ species [56,57]. Meanwhile, in the Co 2p spectrum of Co₃O₄-5% HMNs (Figure 4b), adsorption peaks corresponding to Co²⁺ 2p_{1/2}, Co²⁺ 2p_{3/2}, Co³⁺ 2p_{1/2}, and Co³⁺ 2p_{3/2} were located at 796.63 eV (u_0), 781.51 eV (v_0), 795.20 eV (u), and 780.20 eV (v), respectively. It is noteworthy that, through fitting calculations, the ratio of Co²⁺/(Co²⁺+Co³⁺) in Co₃O₄ NCs and Co₃O₄-5% HMNs was greater than 0.33, due to the presence of oxygen vacancies increasing the content of Co²⁺ [25,58]. Meanwhile, the results also showed that the ratio of Co²⁺/(Co²⁺+Co³⁺) in Co₃O₄-5% HMNs (49.2%) was higher than that in Co₃O₄ NCs (39.1%), indicating that more oxygen vacancies were generated in Co₃O₄-5% HMNs. To further validate this conclusion, the O 1s spectra of both Co₃O₄ NCs and Co₃O₄-5% HMNs were collected and subjected to peak fitting analysis (Figure 4c,d). As illustrated in Figure 4c,d, the O 1s spectra exhibited three distinct peaks at approximately 533.1 eV (O_A), 531.3 eV (O_V), and 529.6 eV (O_L), which were assigned to oxygen species in surface-adsorbed hydroxyl groups, oxygen vacancies, and metal-oxygen bonds, respectively [59,60]. The fitting results (Table S1) reveal that the relative area of the oxygen vacancy (O_V) peak in Co₃O₄-5% HMNs constituted 49.9% of the total O 1s spectrum, significantly higher than that in Co₃O₄ NCs (32.8%). This finding further corroborates that Co₃O₄-5% HMNs possessed a higher concentration of oxygen vacancies compared to Co₃O₄ NCs. The increased concentration of oxygen vacancies in Co₃O₄-5% HMNs primarily originated from unsaturated coordination induced by the exposure of additional edge sites. These vacancies led to a noticeable weakening of Co–O bonds, as evidenced by FTIR spectral analysis [61,62]. In addition, the generation of vacancies could regulate the adsorption of reactants and reaction intermediates and improve the intrinsic reaction activity [53]. Therefore, defect engineering can efficiently modulate the electronic structure of materials, which will contribute to the improvement of OER performance.

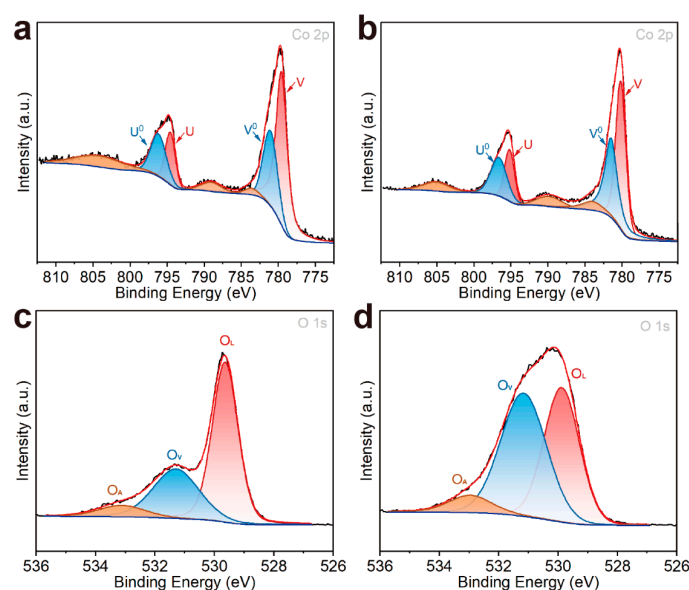


Figure 4. Co 2p XPS spectra of (a) Co₃O₄ NCs and (b) Co₃O₄-5% HMNs; O 1s XPS spectra of (c) Co₃O₄ NCs and (d) Co₃O₄-5% HMNs.

The OER performance of the synthesized electrocatalysts was systematically evaluated in a 1.0 M KOH electrolyte using a standard three-electrode system. Initially, linear sweep voltammetry (LSV) was employed to obtain polarization curves, enabling the comparison of overpotentials (η) among different electrocatalysts at specific current densities. A lower overpotential at identical current density signifies superior electrocatalytic performance [63]. Figure 5a presents the polarization curves of Co_3O_4 HMNs synthesized from precursor solutions containing varying concentrations of hydrogen peroxide (3%, 5%, and 7%). Notably, Co_3O_4 -5% HMNs exhibited the lowest overpotential (330 mV) at a current density of 10 mA cm^{-2} , while deviations from the optimal hydrogen peroxide concentration (either lower or higher) resulted in increased overpotentials. Furthermore, Tafel plots were constructed to analyze the rate of current density increase with respect to overpotential, where a smaller Tafel slope indicated faster kinetics. As shown in Figure 5b, Co_3O_4 -5% HMNs demonstrated the smallest Tafel slope compared to Co_3O_4 -3% HMNs and Co_3O_4 -7% HMNs, confirming that the addition of 5% hydrogen peroxide to the precursor solution optimally enhanced the OER performance of Co_3O_4 -5% HMNs. The enhanced OER performance of Co_3O_4 -5% HMNs was inherently linked to its structure and properties. Next, electrochemical impedance spectroscopy (EIS) testing was conducted to assess the interfacial charge transfer capabilities of the catalysts. In the Nyquist plot, the diameter of the semicircle observed in the high-frequency region corresponds to the charge transfer resistance (R_{ct}), which reflects the kinetics of electron transfer at the electrode-electrolyte interface [64]. As shown in Figure 5c, Co_3O_4 -5% HMNs exhibited a significantly smaller R_{ct} compared to Co_3O_4 -3% HMNs and Co_3O_4 -7% HMNs, demonstrating superior charge transfer kinetics and enhanced electrocatalytic efficiency. Afterwards, the surface vacancy defects of these HMNs were investigated through XPS analysis. For this purpose, O 1s spectra of Co_3O_4 -3% HMNs and Co_3O_4 -7% HMNs were collected, followed by spectral deconvolution (Figure S5). Table S1 summarizes the ratio of O_v derived from the deconvolution analysis of O 1s XPS spectra (Figures 5d and S5). As evident from Table S1, as the concentration of hydrogen peroxide increased, the oxygen vacancy concentration in Co_3O_4 HMNs increased. The above results are primarily attributed to the following: while an appropriate concentration of oxygen vacancies effectively enhances the number of active sites and improves electrical conductivity, excessive oxygen vacancies conversely lead to a deterioration in the material's conductive properties [65–67]. To investigate the influence of crystal facets on OER performance, Co_3O_4 NCs with exclusively exposed (111) facets were synthesized (Figure 2). In comparison, Co_3O_4 -5% HMNs exhibited a lower overpotential of 330 mV at 10 mA cm^{-2} than Co_3O_4 NCs and commercial RuO_2 , as clearly demonstrated in Figure 5d. Meantime, the Tafel plots in Figure 5e also reveal that Co_3O_4 -5% HMNs possessed a smaller Tafel slope (69 mV dec^{-1}) than Co_3O_4 NCs (99 mV dec^{-1}) and commercial RuO_2 (100 mV dec^{-1}). EIS testing (Figure 5f) revealed that Co_3O_4 -5% HMNs exhibited a lower R_{ct} , suggesting excellent charge transfer kinetics, which contributed substantially to the enhanced electrochemical performance (Figure 5g). More significantly, previous characterizations have also revealed that Co_3O_4 -5% HMNs have more oxygen vacancies and weakened Co-O bands compared to Co_3O_4 NCs, which undoubtedly contributed to the enhanced OER performance. Mass activity, which accounts for the influence of catalyst mass, is another critical metric for evaluating OER performance. As depicted in Table S2, Co_3O_4 -5% HMNs achieved a high mass activity of 13.39 A g^{-1} at an overpotential of 350 mV, which was higher than those of Co_3O_4 -3% HMNs (5.84 A g^{-1}), Co_3O_4 -7% HMNs (13.39 A g^{-1}) and Co_3O_4 NCs (0.59 A g^{-1}). Additionally, the turnover frequency (TOF), representing the number of oxygen molecules produced per active site per unit time, provided insights into the intrinsic activity of individual catalytic sites. It can be concluded from Table S3 that Co_3O_4 -5% HMNs obtained the highest TOF value

($11.28 \times 10^{-3} \text{ s}^{-1}$) among all synthesized electrocatalysts. Compared with cobalt-based electrocatalysts reported in recent literature, this catalyst demonstrated outstanding OER performance (Table S4). Finally, chronopotentiometry measurements were performed to evaluate the electrochemical stability of the materials [63]. As illustrated in Figure 5h, Co_3O_4 -5% HMNs maintained stable OER performance for up to 24 h with almost no degradation, demonstrating their excellent durability. To investigate whether the electrocatalyst underwent changes after the reaction, TEM and FTIR were used to characterize its morphology and structure. As clearly demonstrated in Figure S6, the TEM image of post-reaction Co_3O_4 -5% HMNs revealed remarkable morphological stability, with the catalyst maintaining its pristine structural characteristics without significant alteration. The FTIR spectra (Figure S7) reveals that the characteristic absorption peaks corresponding to the Co-O vibrational mode in the post-reaction Co_3O_4 -5% HMNs catalyst remained essentially unchanged, suggesting excellent structural integrity and stability of the catalyst framework throughout the electrochemical process.

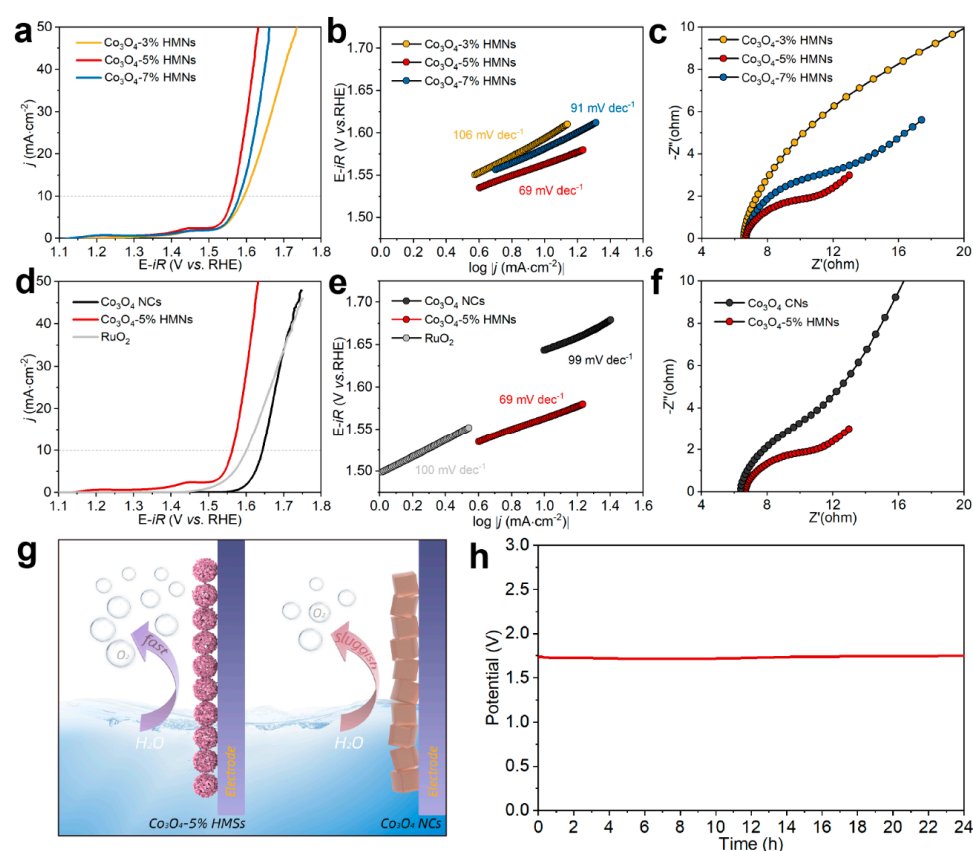


Figure 5. (a) polarization curves, (b) Tafel plots and (c) Nyquist plots of Co_3O_4 -3% HMNs, Co_3O_4 -5% HMNs, Co_3O_4 -7% HMNs; Co_3O_4 -5% HMNs and Co_3O_4 -7% HMNs. (d) polarization curves and (e) Tafel plots of Co_3O_4 -5% HMNs, Co_3O_4 NCs and commercial RuO_2 . (f) Nyquist plots of Co_3O_4 -5% HMNs and Co_3O_4 NCs. (g) Schematic illustration of OER process on Co_3O_4 -5% HMNs and Co_3O_4 NCs. (h) chronopotentiometry curve of Co_3O_4 -5% HMNs for durability test.

Based on the above discussion, the outstanding OER performance of Co_3O_4 -5% HMNs can be primarily attributed to the regulation of dual-engineering strategies and the construction of unique hollow structure. Firstly, the Co_3O_4 nanosheet structure could expose high-index (111) crystal facets, which possessed the biggest dangling bond density and highest surface energy. A higher density of dangling bonds implies a greater number of coordination-unsaturated atoms, which, in turn, serves as a more robust indication of the existence of a larger quantity of oxygen vacancies. The increase in oxygen vacancy

content could not only weaken Co-O bonds but also regulate the adsorption of reactants and reaction intermediates. The weakening of this bond caused the O 2p band to shift upward toward the Fermi level. Therefore, the mobility of oxygen ions was enhanced, and the oxygen exchange processes became more efficient. Secondly, self-assembling these highly active nanosheets into HMNs can effectively prevent the aggregation and stacking of Co₃O₄ nanosheets, thus exposing more edge sites and enhancing the effective contact area with the electrolyte. Thus, the edge sites were more fully exposed, significantly increasing the number of coordination-unsaturated atoms. Furthermore, when nanosheets were assembled into hollow structures, an extensive channel network formed, facilitating electrolyte flow. This significantly expanded the contact area between the structure and the electrolyte, enabling more efficient interaction during electrolysis. All in all, the dual-engineering strategy effectively regulated the electronic structure and micro-geometric structure of Co₃O₄-5% HMNs, synergistically enhancing their OER performance.

3. Materials and Methods

All chemicals, i.e., cobalt chloride hexahydrate (CoCl₂·6H₂O), urea ((NH₂)₂CO), hydrogen peroxide (H₂O₂, 30 wt%), potassium hydroxide (KOH), anhydrous ethanol (C₂H₅OH, ≥99.7%), and deionized water (H₂O, 18.2 MΩ·cm⁻¹ at 25 °C), were of analytical grade and used as received without further purification. The Nafion solution (5 wt%) was obtained from commercial sources.

Co₃O₄ HMNs: Firstly, 0.136 g of hexahydrate cobalt chloride and 0.173 g of urea were sequentially dissolved in 64 mL of deionized water to form a homogeneous and transparent purple red solution. Secondly, a certain amount of hydrogen peroxide solution with the mass fraction of hydrogen peroxide (H₂O₂) in the total solution being 3%, 5%, and 7%, respectively, was added to the above solution to form the final precursor solution. Next, the prepared precursor solutions were transferred to 100 mL stainless steel reaction vessels. The stainless-steel reaction vessels were placed in a drying oven at 160 °C for 20 h and then naturally cooled to room temperature in air. After the reaction, the suspension was separated by centrifugation to obtain a precipitate. These precipitates were then washed with deionized water and ethanol several times. Finally, the washed sample was dried in an 80 °C vacuum oven for 12 h to obtain a black/brown powder, which was Co₃O₄ HMNs. According to the amount of hydrogen peroxide added, the final electrocatalysts obtained were named Co₃O₄-3% HMNs, Co₃O₄-5% HMNs, and Co₃O₄-7% HMNs.

Co₃O₄ nanocubes (NCs): The synthesis of Co₃O₄ NCs was similar to that of Co₃O₄ HMNs, except that no hydrogen peroxide solution was added during the preparation of the precursor solution.

Scanning electron microscopy (SEM) images were acquired by means of a JSM-6700 (JEOL, Akishima, Tokyo, Japan) scanning electron microscope operating at an accelerating voltage of 5.0 kV. Transmission electron microscopy (TEM) images, high-resolution transmission electron microscopy (HRTEM) images, and selected area electron diffraction (SAED) images were obtained using a JEM-2100F (JEOL, Akishima, Tokyo, Japan) transmission electron microscope, which was operated at an accelerating voltage of 200.0 kV. Nitrogen adsorption-desorption measurements were conducted using a Micromeritics ASAP 2020 analyzer (Micromeritics Instrument Corporation, Norcross, GA, USA) to determine the specific surface area and pore size distribution through Brunauer-Emmett-Teller (BET) and Barrett-Joyner-Halenda (BJH) methods, respectively. The crystalline structure was characterized by X-ray powder diffraction (XRD) using a Bruker D8 Advance diffractometer (Bruker AXS, Karlsruhe, Germany) with Cu Kα radiation (λ = 1.5406 Å) at 40 kV and 40 mA. X-ray photoelectron spectroscopy (XPS) was collected by a Thermo K-Alpha+

X-ray photoelectron spectrometer. Fourier transform infrared spectra (FTIR) were obtained by a Perkin Elmer spectrum 100 infrared spectrometer.

The working electrode was prepared through the following procedure: Initially, 5.0 mg of the electrocatalyst was ultrasonically dispersed in 500 μL ethanol for 10 min to achieve a uniform suspension. Subsequently, 30 μL of 5 wt% Nafion solution was added to the suspension, followed by additional sonication for 5 min to ensure complete mixing and formation of a homogeneous catalyst ink. Finally, 20 μL of the optimized catalyst ink was precisely deposited onto a polished glassy carbon electrode (5 mm in diameter) using a micropipette and allowed to dry at room temperature, resulting in a uniform catalyst layer ready for electrochemical testing (Figure S1). In this work, all electrochemical tests were conducted in 1.0 M KOH solution using a three-electrode configuration at ambient temperature on a CHI660E electrochemical workstation. The three-electrode system comprised a graphite electrode used as the counter electrode, a mercury oxide electrode (Hg/HgO) as the reference electrode, and a glassy carbon electrode coated with the electrocatalyst as the working electrode. Polarization curves were collected by linear sweep voltammetry (LSV) at a scan rate of 10 mV s^{-1} , with the potential ranging from 0 to 0.8 V versus Hg/HgO. These LSV curves were subsequently transformed into Tafel plots by graphing overpotential (η) against the logarithm of current density ($\log |j|$). Electrochemical impedance spectroscopy (EIS) measurements were conducted over a frequency range of 100 kHz to 1 Hz at a fixed potential of 0.55 V versus Hg/HgO. Additionally, the electrochemical double-layer capacitance (C_{dl}) was determined using cyclic voltammetry (CV) at scan rates of 10, 30, 50, 70, and 90 mV s^{-1} within a potential window of -0.1 to 0.0 V versus Hg/HgO, ensuring the absence of faradaic processes.

The turnover frequency (TOF) serves as a critical metric for assessing the intrinsic activity of catalysts, providing deeper insights into their OER performance [2,3]. The TOF value quantifies the number of oxygen molecules generated per active site per unit time and can be calculated using the following equation:

$$\text{TOF}(\text{s}^{-1}) = \frac{j \times M_{W,\text{catalyst}}}{F \times n \times m_{\text{catalyst}}} \quad (1)$$

where j represents the current density at a given overpotential of 350 mV (mA cm^{-2}), M_W , catalyst is the molar mass of the synthesized electrocatalyst (g mol^{-1}), F is the Faraday constant ($F = 96,485 \text{ C mol}^{-1}$), n is the number of electrons transferred during the OER process ($n = 4$), and m is the mass loading of the electrocatalyst per geometric electrode area (mg cm^{-2}).

4. Conclusions

In conclusion, this study innovatively synthesized Co_3O_4 hollow microspheres assembled from nanosheets (HMNs) via a dual-engineering strategy, precisely tailoring crystal facet exposure and introducing oxygen vacancies. The Co_3O_4 -5% HMNs achieved remarkable OER performance, requiring only 330 mV overpotential at 10 mA cm^{-2} and featuring a Tafel slope of 69 mV dec^{-1} , outperforming both Co_3O_4 nanocubes (NCs) and commercial RuO_2 . The outstanding catalytic activity resulted from crystal facet engineering exposing high-index (111) facets with high surface energy and defect engineering optimizing Co-O bond energy and reactant adsorption through oxygen vacancies, while the unique hollow structure of HMNs prevented nanosheet stacking, maximized edge site exposure, and facilitated efficient mass transport to accelerate OER kinetics. This research clarifies the structure/performance relationship of Co_3O_4 -based electrocatalysts and presents an effective approach for developing high-performance, low-cost OER catalysts, which are

vital for sustainable hydrogen production, with a scalable synthesis method. The potential application of this approach in other catalytic systems is worthy of further exploration.

Supplementary Materials: The following supporting information can be downloaded at: <https://www.mdpi.com/article/10.3390/molecules30102181/s1>, Figure S1. The polarization curves for the Co₃O₄-5% HMNs with different loading (i. 0.722 mg cm^{−2}, ii. 0.963 mg cm^{−2}, iii. 1.203 mg cm^{−2}).; Figure S2. SEM images of (a) Co₃O₄-3% HMNs and (b) Co₃O₄-7% HMNs.; Figure S3. XPS full spectra of Co₃O₄-5% HMNs and Co₃O₄ NCs.; Figure S4. XRD patterns of Co₃O₄-3% HMNs, Co₃O₄-5% HMNs and Co₃O₄-7% HMNs.; Figure S5. O 1s spectra of Co₃O₄-3% HMNs and Co₃O₄-7% HMNs.; Figure S6. TEM image of Co₃O₄-5% HMNs after OER.; Figure S7. FTIR spectra of Co₃O₄-5% HMNs before and after OER.; Table S1. The ratio of Ov obtained from O 1s spectra of Co₃O₄-3% HMNs, Co₃O₄-5% HMNs, Co₃O₄-7% HMNs and Co₃O₄ NCs.; Table S2. The mass activity of samples.; Table S3. The TOF of samples.; Table S4. Comparison with OER performance of the electrocatalysts in literature [68–79].

Author Contributions: Conceptualization, H.W., J.Q.; methodology, Y.C., S.Y.; validation, H.W. Z.W. and J.Z.; formal analysis, H.W. and J.Q.; investigation, S.Y. and Y.C.; data curation, S.Y.; writing—original draft preparation, H.W.; writing—review and editing, J.Q., S.C.; funding acquisition, S. C.; supervision, J.Q., S.C. and H.W.; All authors have read and agreed to the published version of the manuscript.

Funding: This research was funded by the National Natural Science Foundation of China (52201159).

Institutional Review Board Statement: Not applicable.

Informed Consent Statement: Not applicable.

Data Availability Statement: The original contributions presented in this study are included in the article/Supplementary Materials. Further inquiries can be directed to the corresponding authors.

Conflicts of Interest: The authors declare no conflict of interest.

References

1. Zhang, Y.; Yao, D.; Liu, J.; Wang, Z.; Wang, L. Advancing strategies on green H₂ production via water electrocatalysis: Bridging the benchtop research with industrial scale-up. *Microstructures* **2024**, *4*, 2024020. [\[CrossRef\]](#)
2. Nguyen, T.; Tekalgne, M.; Le, Q.; Tran, C.; Ahn, S.; Kim, S. Recent progress and strategies of non-noble metal electrocatalysts based on MoS₂/MOF for the hydrogen evolution reaction in water electrolysis: An overview. *Microstructures* **2024**, *4*, 2024046. [\[CrossRef\]](#)
3. Mane, R.; Mane, S.; Somkuwar, V.; Thombre, N.; Patwardhan, A.; Jha, N. A novel hierarchically hybrid structure of MXene and bi-ligand ZIF-67 based trifunctional electrocatalyst for zinc-air battery and water splitting. *Battery Energy* **2023**, *2*, 20230019. [\[CrossRef\]](#)
4. Nguyen, T.; Tekalgne, M.; Nguyen, T.; Le, Q.; Ahn, S.; Kim, S. Electrocatalysts based on MoS₂ and WS₂ for hydrogen evolution reaction: An overview. *Battery Energy* **2023**, *2*, 20220057. [\[CrossRef\]](#)
5. Yang, N.; He, T.; Chen, X.; He, Y.; Zhou, T.; Zhang, G.; Liu, Q. TiO₂-based heterojunctions for photocatalytic hydrogen evolution reaction. *Microstructures* **2024**, *4*, 2024042. [\[CrossRef\]](#)
6. Yan, J.; Wu, R.; Jin, G.; Jia, L.; Feng, G.; Tong, X. The hybrid Pt nanoclusters/Ru nanowires catalysts accelerating alkaline hydrogen evolution reaction. *Adv. Powder Mater.* **2024**, *3*, 100214. [\[CrossRef\]](#)
7. Yan, M.; Chen, S.; Wu, S.; Zhou, X.; Fu, S.; Wang, D.; Kübel, C.; Hahn, H.; Lan, S.; Feng, T. Enhanced activity and durability of FeCoCrMoCBy nanoglass in acidic hydrogen evolution reaction. *J. Mater. Sci. Technol.* **2024**, *170*, 212–220. [\[CrossRef\]](#)
8. Lin, L.; Ding, Z.; Karkera, G.; Diemant, T.; Chen, D.; Fichtner, M.; Hahn, H.; Aghassi-Hagmann, J.; Breitung, B.; Schweidler, S. Layered high-entropy sulfides: Boosting electrocatalytic performance for hydrogen evolution reaction by cocktail effects. *Mater. Futures* **2024**, *3*, 045102. [\[CrossRef\]](#)
9. Xu, X.; Qiao, F.; Liu, Y.; Liu, W. Preparation of Cu(OH)₂/Cu₂S arrays for enhanced hydrogen evolution reaction. *Battery Energy* **2024**, *3*, 20230060. [\[CrossRef\]](#)
10. Shu, C.; Cao, J.; Gan, Z.; Qiu, P.; Chen, Z.; Guanwu, L.; Chen, Z.; Deng, C.; Tang, W. Synergistic effect between Co single atoms and Pt nanoparticles for efficient alkaline hydrogen evolution. *Mater. Futures* **2024**, *3*, 035101. [\[CrossRef\]](#)

11. Xiao, Z.; Zhou, W.; Yang, B.; Liao, C.; Kang, Q.; Chen, G.; Liu, M.; Liu, X.; Ma, R.; Zhang, N. Tuned d-band states over lanthanum doped nickel oxide for efficient oxygen evolution reaction. *Nano Mater. Sci.* **2023**, *5*, 228–236. [[CrossRef](#)]
12. Mu, Y.; Pei, X.; Zhao, Y.; Dong, X.; Kou, Z.; Cui, M.; Meng, C.; Zhang, Y. In situ confined vertical growth of $\text{Co}_{2.5}\text{Ni}_{0.5}\text{Si}_2\text{O}_5(\text{OH})_4$ nanoarrays on rGO for an efficient oxygen evolution reaction. *Nano Mater. Sci.* **2023**, *5*, 351–360. [[CrossRef](#)]
13. Liu, G.; Xu, Y.; Yang, T.; Jiang, L. Recent advances in electrocatalysts for seawater splitting. *Nano Mater. Sci.* **2023**, *5*, 101–116. [[CrossRef](#)]
14. Wang, S.; Zhu, S.; Kang, Z.; Wang, X.; Deng, Z.; Hu, K.; Hu, J.; Liu, X.; Wang, G.; Zang, G.; et al. Particle size-controlled oxygen reduction and evolution reaction nanocatalysts regulate $\text{Ru}(\text{bpy})_3^{2+}$'s dual-potential electrochemiluminescence for sandwich immunoassay. *Research* **2023**, *6*, 0117. [[CrossRef](#)] [[PubMed](#)]
15. Liu, Q.; Zhao, F.; Yang, X.; Zhu, J.; Yang, S.; Chen, L.; Zhao, P.; Wang, Q.; Zhang, Q. Constructing interlaced network structure by grain boundary corrosion methods on CrCoNiFe alloy for high-performance oxygen evolution reaction and urea oxidation reaction. *J. Mater. Sci. Technol.* **2024**, *203*, 97–107. [[CrossRef](#)]
16. Zhang, H.; Zhang, Q.; Zeng, X. Construction of multiple heterogeneous interfaces and oxygen evolution reaction of hollow CoFe bimetallic phosphides derived from MOF template. *Prog. Nat. Sci. Mater. Int.* **2024**, *34*, 913–920. [[CrossRef](#)]
17. Suen, N.-T.; Hung, S.-F.; Quan, Q.; Zhang, N.; Xu, Y.-J.; Chen, H.M. Electrocatalysis for the oxygen evolution reaction: Recent development and future perspectives. *Chem. Soc. Rev.* **2017**, *46*, 337–365. [[CrossRef](#)] [[PubMed](#)]
18. Xie, X.; Du, L.; Yan, L.; Park, S.; Qiu, Y.; Sokolowski, J.; Wang, W.; Shao, Y. Oxygen Evolution Reaction in Alkaline Environment: Material Challenges and Solutions. *Adv. Funct. Mater.* **2022**, *32*, 2110036. [[CrossRef](#)]
19. Wang, H.; Sun, F.; Qi, J.; Zhang, D.; Sun, H.; Wang, Q.; Li, Z.; Wu, Y.A.; Hu, Z.; Wang, B. Recent progress on layered double hydroxides: Comprehensive regulation for enhanced oxygen evolution reaction. *Mater. Today Energy* **2022**, *27*, 101036. [[CrossRef](#)]
20. Reier, T.; Nong, H.N.; Teschner, D.; Schlögl, R.; Strasser, P. Electrocatalytic Oxygen Evolution Reaction in Acidic Environments—Reaction Mechanisms and Catalysts. *Adv. Energy Mater.* **2017**, *7*, 1601275. [[CrossRef](#)]
21. Li, L.; Wang, P.; Shao, Q.; Huang, X. Recent Progress in Advanced Electrocatalyst Design for Acidic Oxygen Evolution Reaction. *Adv. Mater.* **2021**, *33*, 2004243. [[CrossRef](#)] [[PubMed](#)]
22. Kim, G.K.; Choi, Y.H. Electrocatalytic properties of Co_3O_4 prepared on carbon fibers by Thermal metal-organic deposition for the oxygen evolution reaction in alkaline. *Nanomaterials* **2023**, *13*, 1021. [[CrossRef](#)] [[PubMed](#)]
23. Zhang, S.L.; Guan, B.Y.; Lu, X.F.; Xi, S.; Du, Y.; Lou, X.W. Metal Atom-Doped Co_3O_4 Hierarchical Nanoplates for Electrocatalytic Oxygen Evolution. *Adv. Mater.* **2020**, *32*, 2002235. [[CrossRef](#)]
24. Wang, C.; Deng, R.; Guo, M.; Zhang, Q. Recent progress of advanced Co_3O_4 -based materials for electrocatalytic oxygen evolution reaction in acid: From rational screening to efficient design. *Int. J. Hydrogen Energy* **2023**, *48*, 31920–31942. [[CrossRef](#)]
25. Sondermann, L.; Jiang, W.; Shviro, M.; Spieß, A.; Woschko, D.; Rademacher, L.; Janiak, C. Nickel-based metal-organic frameworks as electrocatalysts for the oxygen evolution reaction (OER). *Molecules* **2022**, *27*, 1241. [[CrossRef](#)]
26. Trębala, M.; Łamacz, A. Modern catalytic materials for the oxygen evolution reaction. *Molecules* **2025**, *30*, 1656. [[CrossRef](#)]
27. Koza, J.A.; He, Z.; Miller, A.S.; Switzer, J.A. Electrodeposition of Crystalline Co_3O_4 —A Catalyst for the Oxygen Evolution Reaction. *Chem. Mater.* **2012**, *24*, 3567–3573. [[CrossRef](#)]
28. Li, Q.; Sun, F.; Zhang, D.; Sun, H.; Wang, Q.; Qi, J.; Wang, H.; Li, Z.; Hu, Z.; Wang, B. Recent progress of hollow structure platform in assisting oxygen evolution reaction. *Chem. Eng. J.* **2023**, *452*, 139232. [[CrossRef](#)]
29. Huang, K.; Sun, Y.; Zhang, Y.; Wang, X.; Zhang, W.; Feng, S. Hollow-Structured Metal Oxides as Oxygen-Related Catalysts. *Adv. Mater.* **2019**, *31*, 1801430. [[CrossRef](#)]
30. Wang, C.; Zhang, Q.; Yan, B.; You, B.; Zheng, J.; Feng, L.; Zhang, C.; Jiang, S.; Chen, W.; He, S. Facet Engineering of Advanced Electrocatalysts Toward Hydrogen/Oxygen Evolution Reactions. *Nano-Micro Lett.* **2023**, *15*, 52. [[CrossRef](#)]
31. Wang, H.; Fan, W.; Yang, S.; Gong, G.; Chen, S.; Jiao, L.; You, F.; Qi, J. Deeply understanding electrocatalytic oxygen evolution reaction from the perspective of defect structures. *Chem. Eng. J.* **2024**, *499*, 156124. [[CrossRef](#)]
32. Fang, L.; Jiang, Z.; Xu, H.; Liu, L.; Guan, Y.; Gu, X.; Wang, Y. Crystal-plane engineering of NiCo_2O_4 electrocatalysts towards efficient overall water splitting. *J. Catal.* **2018**, *357*, 238–246. [[CrossRef](#)]
33. Zhang, Y.; Ding, F.; Deng, C.; Zhen, S.; Li, X.; Xue, Y.; Yan, Y.-M.; Sun, K. Crystal plane-dependent electrocatalytic activity of Co_3O_4 toward oxygen evolution reaction. *Catal. Commun.* **2015**, *67*, 78–82. [[CrossRef](#)]
34. Wang, C.; Liu, D.; Zhang, K.; Xu, H.; Yu, R.; Wang, X.; Du, Y. Defect and Interface Engineering of Three-Dimensional Open Nanonetcage Electrocatalysts for Advanced Electrocatalytic Oxygen Evolution Reaction. *ACS Appl. Mater. Interfaces* **2022**, *14*, 38669–38676. [[CrossRef](#)]
35. Wang, H.; Ma, Q.; Sun, F.; Shao, Y.; Zhang, D.; Sun, H.; Li, Z.; Wang, Q.; Qi, J.; Wang, B. Oxygen vacancy and interface effect adjusted hollow dodecahedrons for efficient oxygen evolution reaction. *Molecules* **2023**, *28*, 5620. [[CrossRef](#)] [[PubMed](#)]
36. Zhang, R.; Pan, L.; Guo, B.; Huang, Z.-F.; Chen, Z.; Wang, L.; Zhang, X.; Guo, Z.; Xu, W.; Loh, K.P.; et al. Tracking the Role of Defect Types in Co_3O_4 Structural Evolution and Active Motifs during Oxygen Evolution Reaction. *J. Am. Chem. Soc.* **2023**, *145*, 2271–2281. [[CrossRef](#)]

37. Wang, X.; Wu, X.-L.; Guo, Y.-G.; Zhong, Y.; Cao, X.; Ma, Y.; Yao, J. Synthesis and Lithium Storage Properties of Co_3O_4 Nanosheet-Assembled Multishelled Hollow Spheres. *Adv. Funct. Mater.* **2010**, *20*, 1680–1686. [\[CrossRef\]](#)
38. Xu, M.; Xia, Q.; Yue, J.; Zhu, X.; Guo, Q.; Zhu, J.; Xia, H. Rambutan-Like Hybrid Hollow Spheres of Carbon Confined Co_3O_4 Nanoparticles as Advanced Anode Materials for Sodium-Ion Batteries. *Adv. Funct. Mater.* **2019**, *29*, 1807377. [\[CrossRef\]](#)
39. Yu, X.; Wu, J.; Zhang, A.; Xue, L.; Wang, Q.; Tian, X.; Shan, S.; Zhong, C.-J.; Zeng, S. Hollow copper-ceria microspheres with single and multiple shells for preferential CO oxidation. *CrystEngComm* **2019**, *21*, 3619–3626. [\[CrossRef\]](#)
40. Wang, H.; Qi, J.; Yang, N.; Cui, W.; Wang, J.; Li, Q.; Zhang, Q.; Yu, X.; Gu, L.; Li, J.; et al. Dual-Defects Adjusted Crystal-Field Splitting of $\text{LaCo}_{1-x}\text{Ni}_x\text{O}_{3-\delta}$ Hollow Multishelled Structures for Efficient Oxygen Evolution. *Angew. Chem. Int. Ed.* **2020**, *59*, 19691–19695. [\[CrossRef\]](#)
41. Fang, L.; Xie, Y.; Yang, Y.; Zhu, B.; Wang, Y.; Liu, M.; Zhao, K.; Zhao, H.; Zhang, J. Interfacial Electronic Modulation of Multishelled CoP Hollow Spheres via Surface Reconstruction for High-Efficient Hydrogen Evolution Reaction. *ACS Appl. Energy Mater.* **2020**, *3*, 309–318. [\[CrossRef\]](#)
42. Wang, H.; Zhang, D.; Sun, H.; Wang, Q.; Li, Z.; Qi, J.; Wang, B. Confinement amorphous cobalt-nickel oxide polyhedral yolk-shell structures for enhanced oxygen evolution performance. *Appl. Surf. Sci.* **2023**, *613*, 156088. [\[CrossRef\]](#)
43. Zheng, Y.; Gao, R.; Zheng, L.; Sun, L.; Hu, Z.; Liu, X. Ultrathin Co_3O_4 Nanosheets with Edge-Enriched {111} Planes as Efficient Catalysts for Lithium–Oxygen Batteries. *ACS Catal.* **2019**, *9*, 3773–3782. [\[CrossRef\]](#)
44. Shan, Z.W.; Adesso, G.; Cabot, A.; Sherburne, M.P.; Syed Asif, S.A.; Warren, O.L.; Chrzan, D.C.; Minor, A.M.; Alivisatos, A.P. Ultrahigh stress and strain in hierarchically structured hollow nanoparticles. *Nat. Mater.* **2008**, *7*, 947–952. [\[CrossRef\]](#)
45. Lai, X.; Halpert, J.E.; Wang, D. Recent advances in micro-/nano-structured hollow spheres for energy applications: From simple to complex systems. *Energy Environ. Sci.* **2012**, *5*, 5604–5618. [\[CrossRef\]](#)
46. Liu, L.; Jiang, Z.; Fang, L.; Xu, H.; Zhang, H.; Gu, X.; Wang, Y. Probing the Crystal Plane Effect of Co_3O_4 for Enhanced Electrocatalytic Performance toward Efficient Overall Water Splitting. *ACS Appl. Mater. Interfaces* **2017**, *9*, 27736–27744. [\[CrossRef\]](#)
47. Alam, S.; Yamashita, H.; Verma, P. Unveiling the Critical Role of High-/Low-Index Facets in Nanostructured Energy Materials for Enhancing the Photoelectrochemical Water Splitting. *ChemCatChem* **2024**, *30*, e202401672. [\[CrossRef\]](#)
48. Sinha, P.; Datar, A.; Jeong, C.; Deng, X.; Chung, Y.G.; Lin, L.-C. Surface Area Determination of Porous Materials Using the Brunauer–Emmett–Teller (BET) Method: Limitations and Improvements. *J. Phys. Chem. C* **2019**, *123*, 20195–20209. [\[CrossRef\]](#)
49. Liu, W.; Liu, R.; Zhang, X. Controllable synthesis of 3D hierarchical Co_3O_4 catalysts and their excellent catalytic performance for toluene combustion. *Appl. Surf. Sci.* **2020**, *507*, 145174. [\[CrossRef\]](#)
50. Xiong, S.; Lin, M.; Wang, L.; Liu, S.; Weng, S.; Jiang, S.; Xu, Y.; Jiao, Y.; Chen, J. Defects-type three-dimensional Co_3O_4 nanomaterials for energy conversion and low temperature energy storage. *Appl. Surf. Sci.* **2021**, *546*, 149064. [\[CrossRef\]](#)
51. Wang, Y.-Z.; Zhao, Y.-X.; Gao, C.-G.; Liu, D.-S. Preparation and catalytic performance of Co_3O_4 catalysts for low-temperature CO oxidation. *Catal. Lett.* **2007**, *116*, 136–142. [\[CrossRef\]](#)
52. Wang, H.; Zhang, Q.; Sun, F.; Qi, J.; Zhang, D.; Sun, H.; Li, Z.; Wang, Q.; Wang, B. Construction of $\text{Co}_3\text{O}_4/\text{CeO}_2$ heterostructure nanoflowers facilitates deployment of oxygen defects to enhance the oxygen evolution kinetics. *J. Alloys Compd.* **2023**, *933*, 167700. [\[CrossRef\]](#)
53. Li, F.; Ai, H.; Liu, D.; Lo, K.H.; Pan, H. An enhanced oxygen evolution reaction on 2D CoOOH via strain engineering: An insightful view from spin state transition. *J. Mater. Chem. A* **2021**, *9*, 17749–17759. [\[CrossRef\]](#)
54. Zhao, Z.; Chang, H.; Wang, R.; Du, P.; He, X.; Yang, J.; Zhang, X.; Huang, K.; Fan, D.; Wang, Y.; et al. Activity Origin and Catalyst Design Principles for Electrocatalytic Oxygen Evolution on Layered Transition Metal Oxide with Halogen Doping. *Small Struct.* **2021**, *2*, 2100069. [\[CrossRef\]](#)
55. Guo, J.; Wang, G.; Cui, S.; Xia, B.; Liu, Z.; Zang, S.-Q. Vacancy and strain engineering of Co_3O_4 for efficient water oxidation. *J. Colloid Interface Sci.* **2023**, *629*, 346–354. [\[CrossRef\]](#)
56. Yang, J.; Liu, Y.; Liu, Y.; Huang, Y.; Wang, K.; Liu, M.; Li, W. Enhanced Co_3O_4 Nanoflakes Reactivity via Integrated Al-Doping and Metal Vacancy Engineering for Large Capacity Li- CO_2 Batteries. *Nano Energy* **2024**, *129*, 109979. [\[CrossRef\]](#)
57. Zhang, Q.; Yang, P.; Zhang, H.; Zhao, J.; Shi, H.; Huang, Y.; Yang, H. Oxygen vacancies in Co_3O_4 promote CO_2 photoreduction. *Appl. Catal. B: Environ.* **2022**, *300*, 120729. [\[CrossRef\]](#)
58. Xie, F.; Guo, J.-F.; Wang, H.-T.; Chang, N. Enhancing visible light photocatalytic activity by transformation of $\text{Co}^{3+}/\text{Co}^{2+}$ and formation of oxygen vacancies over rationally Co doped ZnO microspheres. *Colloids Surf. A: Physicochem. Eng. Asp.* **2022**, *636*, 128157. [\[CrossRef\]](#)
59. Wang, H.; Wang, D.; Sun, C.; Zhao, X.; Xu, C.; Li, Z.; Hou, Y.; Lei, L.; Yang, B.; Duan, X. Oriented generation of 1O_2 from peroxymonosulfate via Co_3O_4 facet engineering. *Appl. Catal. B Environ. Energy* **2025**, *364*, 124854. [\[CrossRef\]](#)
60. Xu, H.; Cao, J.; Shan, C.; Wang, B.; Xi, P.; Liu, W.; Tang, Y. MOF-Derived Hollow CoS Decorated with CeO_x Nanoparticles for Boosting Oxygen Evolution Reaction Electrocatalysis. *Angew. Chem. Int. Ed.* **2018**, *57*, 8654–8658. [\[CrossRef\]](#)
61. Kuznetsov, D.A.; Naeem, M.A.; Kumar, P.V.; Abdala, P.M.; Fedorov, A.; Müller, C.R. Tailoring Lattice Oxygen Binding in Ruthenium Pyrochlores to Enhance Oxygen Evolution Activity. *J. Am. Chem. Soc.* **2020**, *142*, 7883–7888. [\[CrossRef\]](#)

62. Chen, H.; Chen, S.; Zhang, Z.; Sheng, L.; Zhao, J.; Fu, W.; Xi, S.; Si, R.; Wang, L.; Fan, M.; et al. Single-Atom-Induced Adsorption Optimization of Adjacent Sites Boosted Oxygen Evolution Reaction. *ACS Catal.* **2022**, *12*, 13482–13491. [\[CrossRef\]](#)
63. Wang, Y.; Yan, D.; El Hankari, S.; Zou, Y.; Wang, S. Recent Progress on Layered Double Hydroxides and Their Derivatives for Electrocatalytic Water Splitting. *Adv. Sci.* **2018**, *5*, 1800064. [\[CrossRef\]](#)
64. Ma, T.Y.; Dai, S.; Jaroniec, M.; Qiao, S.Z. Metal–Organic Framework Derived Hybrid Co₃O₄-Carbon Porous Nanowire Arrays as Reversible Oxygen Evolution Electrodes. *J. Am. Chem. Soc.* **2014**, *136*, 13925–13931. [\[CrossRef\]](#)
65. Zhuang, L.; Ge, L.; Yang, Y.; Li, M.; Jia, Y.; Yao, X.; Zhu, Z. Ultrathin Iron-Cobalt Oxide Nanosheets with Abundant Oxygen Vacancies for the Oxygen Evolution Reaction. *Adv. Mater.* **2017**, *29*, 1606793. [\[CrossRef\]](#)
66. Zhang, X.; Liu, X.; Zeng, Y.; Tong, Y.; Lu, X. Oxygen Defects in Promoting the Electrochemical Performance of Metal Oxides for Supercapacitors: Recent Advances and Challenges. *Small Methods* **2020**, *4*, 1900823. [\[CrossRef\]](#)
67. Ji, Q.; Bi, L.; Zhang, J.; Cao, H.; Zhao, X.S. The role of oxygen vacancies of ABO₃ perovskite oxides in the oxygen reduction reaction. *Energy Environ. Sci.* **2020**, *13*, 1408–1428. [\[CrossRef\]](#)
68. Xue, Z.H.; Su, H.; Yu, Q.Y.; Zhang, B.; Wang, H.H.; Li, X.H.; Chen, J.S. Janus Co/CoP nanoparticles as efficient mott-schottky electrocatalysts for overall water splitting in wide pH range. *Adv. Energy Mater.* **2017**, *7*, 1602355. [\[CrossRef\]](#)
69. Liu, H.; Ma, F.; Xu, C.; Yang, L.; Du, Y.; Wang, P.; Yang, S.; Zhen, L. Sulfurizing-induced hollowing of Co₉S₈ microplates with nanosheet units for highly efficient water oxidation. *ACS Appl. Mater. Inter.* **2017**, *9*, 11634–11641. [\[CrossRef\]](#)
70. Zhang, R.; Ke, W.; Chen, S.; Yue, X.; Hu, Z.; Ning, T. Phase evolution of vulcanized Co₃O₄ catalysts during oxygen evolution reaction. *Appl. Surf. Sci.* **2021**, *546*, 148819. [\[CrossRef\]](#)
71. Malik, B.; Anantharaj, S.; Karthick, K.; Pattanayak, D.K.; Kundu, S. Magnetic CoPt nanoparticle-decorated ultrathin Co(OH)₂ nanosheets: An efficient bi-functional water splitting catalyst. *Catal. Sci. Technol.* **2017**, *7*, 2486–2497. [\[CrossRef\]](#)
72. Yang, G.; Xiang, H.; Rauf, M.; Mi, H.; Ren, X.; Zhang, P.; Li, Y. Plasma enhanced atomic-layer-deposited nickel oxide on Co₃O₄ arrays as highly active electrocatalyst for oxygen evolution reaction. *J. Power Sources* **2021**, *481*, 228925. [\[CrossRef\]](#)
73. Lu, Y.; Li, C.; Zhang, Y.; Cao, X.; Xie, G.; Wang, M.; Peng, D.; Huang, K.; Zhang, B.; Wang, T.; et al. Engineering of cation and anion vacancies in Co₃O₄ thin nanosheets by laser irradiation for more advancement of oxygen evolution reaction. *Nano Energy* **2021**, *83*, 105800. [\[CrossRef\]](#)
74. Bao, W.; Xiao, L.; Zhang, J.; Jiang, P.; Zou, X.; Yang, C.; Hao, X.; Ai, T. Electronic and structural engineering of NiCo₂O₄/Ti electrocatalysts for efficient oxygen evolution reaction. *Int. J. Hydrogen Energy* **2021**, *46*, 10259–10267. [\[CrossRef\]](#)
75. Saad, A.; Liu, D.; Wu, Y.; Song, Z.; Li, Y.; Najam, T.; Zong, K.; Tsiakaras, P.; Cai, X. Ag nanoparticles modified crumpled borophene supported Co₃O₄ catalyst showing superior oxygen evolution reaction (OER) performance. *Appl. Catal. B-Environ.* **2021**, *298*, 120529. [\[CrossRef\]](#)
76. Wang, X.; Zhou, Y.; Luo, J.; Sun, F.; Zhang, J. Synthesis of V-doped urchin-like NiCo₂O₄ with rich oxygen vacancies for electrocatalytic oxygen evolution reactions. *Electrochim. Acta* **2022**, *406*, 139800. [\[CrossRef\]](#)
77. Hang, L.; Sun, Y.; Men, D.; Liu, S.; Zhao, Q.; Cai, W.; Li, Y. Hierarchical micro/nanostructured C doped Co/Co₃O₄ hollow spheres derived from PS@Co(OH)₂ for the oxygen evolution reaction. *J. Mater. Chem. A* **2017**, *5*, 11163–11170. [\[CrossRef\]](#)
78. Jiang, J.; Xu, J.; Wang, W.; Zhang, L.; Xu, G. Phosphate ion-functionalized CoS with hexagonal bipyramid structures from a metal–organic framework: Bifunctionality towards supercapacitors and oxygen evolution reaction. *Chem.-Eur. J.* **2020**, *26*, 14903–14911. [\[CrossRef\]](#)
79. Hu, H.; Guan, B.; Xia, B.; Lou, X.W. Designed formation of Co₃O₄/NiCo₂O₄ double-shelled nanocages with enhanced pseudocapacitive and electrocatalytic properties. *J. Am. Chem. Soc.* **2015**, *137*, 5590–5595. [\[CrossRef\]](#)

Disclaimer/Publisher’s Note: The statements, opinions and data contained in all publications are solely those of the individual author(s) and contributor(s) and not of MDPI and/or the editor(s). MDPI and/or the editor(s) disclaim responsibility for any injury to people or property resulting from any ideas, methods, instructions or products referred to in the content.